A Unification of LoS, Non-LoS and Quasi-LoS Signal Propagation in Wireless Channels

Jonathan W. Browning, *Member, IEEE,* Simon L. Cotton, *Senior Member, IEEE,* Paschalis C. Sofotasios, *Senior Member, IEEE,* David Morales-Jimenez, *Senior Member, IEEE,* and Michel Daoud Yacoub, *Member, IEEE*

***Abstract*—The modeling of wireless communications channels is often broken down into two distinct states, defined according to the optical viewpoints of the transmitter (TX) and receiver (RX) antennas, namely line-of-sight (LoS) and non-LoS (NLoS). Movement by the TX, RX, both and/or objects in the surrounding environment means that channel conditions may transition between LoS and NLoS leading to a third state of signal propagation, namely quasi-LoS (QLoS). Unfortunately, this state is largely ignored in the analysis of signal propagation in wireless channels. We therefore propose a new statistical framework that unifies signal propagation for LoS, NLoS, and QLoS channel conditions, leading to the creation of the Three State Model (TSM). The TSM has a strong physical motivation, whereby the signal propagation mechanisms underlying each state are considered to be similar to those responsible for Rician fading. However, in the TSM, the dominant signal component, if present, can be subject to shadowing. To support the use of the TSM, we develop novel formulations for the probability density functions of the in-phase and quadrature components of the complex received signal, the received signal envelope, and the received signal phase. Additionally, we derive an expression for the complex autocorrelation function of the TSM, which will be of particular importance in understanding and simulating its time correlation properties. Finally, we show that the TSM provides a good fit to field measurements obtained for two different body-centric wireless channels operating at 2.45 GHz, which are known to be subject to the phenomena underlying the TSM.**

***Index Terms*—Body-centric communications, channel characterization, multimodal, non-isotropic, shadowed fading, statistics, time-series analysis.**

I. Introduction

SIGNAL propagation in wireless channels is often assumed to take place through one of four physical mechanisms, namely line-of-sight (LoS) propagation (or free space propagation), reflection, diffraction, and scattering [1]. Determining how these mechanisms interact and contribute to the overall signal reception is non-trivial. It depends on a number of factors including the geometrical configuration of the transmitter (TX) and receiver (RX) relative to one another, the characteristics of the operating environment, the presence of blocking and scattering objects, and the frequency of operation, to name but a few. LoS propagation and specular reflection tend to be the dominant processes in terms of the overall power contribution [1]. While diffraction and especially scattering are critical for supporting communications in non-LoS (NLoS) scenarios where there may be no dominant signal path between the TX and RX [2]. In many practical wireless applications, the transition between LoS and NLoS channel conditions is rarely discrete and involves a third state referred to as quasi-LoS (QLoS) [3], obstructed LoS [4]–[6] or near LoS [7], [8]. In this transitory phase, there may be a reconstitution of the weighting of each of the propagation mechanisms listed above as the channel moves from LoS to NLoS and vice versa. For example, by moving from LoS, through QLoS to NLoS, a reduction in the power contributed by the dominant component can be expected (through shadowing), meaning that the link will become increasingly reliant on the mechanisms associated with NLoS propagation. Furthermore, new contributing signal components and changes in the direction of arrival (DoA) may emerge as the geometrical propagation paths evolve.

The signal propagation picture described above is a complicated one, even for each of the three states individually. Acknowledging this, it is therefore unsurprising that researchers tend to favor the use of statistical models [2], [9], [10] as opposed to analytical models [11]–[13], which become difficult to use beyond the simplest scenarios. Chief among the most commonly adopted models for LoS and NLoS propagation are the Rician [9] and Rayleigh [2] fading models, respectively. In a Rician fading channel, the received signal is composed of a LoS (or dominant) signal component and a scattered signal contribution [9]. Here, the in-phase and quadrature components of the complex received signal are assumed to follow a Gaussian distribution with non-zero mean and identical variance. In the absence of a dominant signal component, the Rician fading model becomes equivalent to the Rayleigh fading model, such that the received signal is composed only of scattered contributions. Both of these models have been used extensively throughout the literature for many years [14]–[21]; nonetheless, for many emergent applications, this may lead to an oversimplification of the signal propagation problem. As a consequence, the realistic evaluation of the performance of wireless communication systems with stringent quality of service requirements becomes detrimentally problematic.

It has been observed through field measurements that the complicated nature of propagation in applications such as in-

J. W. Browning, and S. L. Cotton are with the Centre for Wireless Innovation, ECIT Institute, Queen's University Belfast, Belfast, BT3 9DT, U.K. (e-mail: j.browning@qub.ac.uk; simon.cotton@qub.ac.uk).

P. C. Sofotasios is with the Center for Cyber-Physical Systems, Department of Electrical and Computer Engineering, Khalifa University, Abu Dhabi, UAE, and also with the Department of Electrical Engineering, Tampere University, 33101 Tampere, Finland (e-mail: p.sofotasios@ieee.org).

D. Morales-Jimenez is with the Department of Signal Theory, Networking and Communications, University of Granada, 18071 Granada, Spain (e-mail: dmorales@ugr.es).

M. D. Yacoub is with the Wireless Technology Laboratory, School of Electrical and Computer Engineering, University of Campinas, Campinas 13083-970, Brazil (e-mail: mdyacoub@unicamp.br).

body area networks [22]–[24], device-to-device communications [24], [25], vehicle-to-vehicle communications [26], [27], and unmanned aerial vehicle communications [28], [29] can lead to multimodal behavior in their first-order statistics. Yet, unfortunately, neither the Rayleigh nor Rician fading models, in their native form, offer the flexibility to encapsulate the transitionary behavior of the channel statistics observed in these use cases. In this context, a recently proposed amplitude fading model that can encapsulate bimodal behavior in the statistics of the channel model is the fluctuating two-ray model [30], which considers two shadowed specular components and a scattered signal component. Another model which is bimodal in nature, is the alternate Rician shadowed (ARS) fading model [31], which uses a mixture of two shadowed Rician distributions to represent LoS and NLoS propagation conditions, whereby the shadowing remains constant across both. Although it was shown to provide a good fit to empirical data, the assumption that shadowing will be constant across both LoS and NLoS states, does not seem intuitive for most practical scenarios. Markov processes have also been utilized to model wireless communications experiencing transitionary behavior, such as the Gilbert-Elliott (GE) model [32], [33]. The GE model is comprised of a two-state Markov process and has been used to characterise burst-noise channels [32], [33]. However, using a two-state Markov process has limitations, for instance when the received signal experiences dramatic changes [34], [35]. As an extension, the finite-state Markov channel (FSMC) model was proposed [34] and later used to model Rayleigh faded channels [35]. Application of the FSMC model is non-trivial and is hampered further by the fact that model only considers Rayleigh faded states. This means that it will be unsuitable for representing the more intricate fading conditions that may arise in many emergent wireless applications, such as those considered here.

Notably, the characteristics of the received signal envelope reveal only part of the overall channel picture. Of critical importance are also the statistics of the received signal phase and those of the in-phase and quadrature components of the complex received signal. The phase properties of the received signal are of particular importance. For example, they are used in the design and synchronization of coherent receivers [36], and in the detection of *M*-ary phase shift keying signal constellations [37]. As a step of convenience some existing models assume that the phase follows the circular uniform distribution [31]. However, it has recently been shown that when the dominant component fluctuates, it can have a significant impact on the distribution of the signal phase [38], leading to cases which are far from uniform. It is not only the first-order characteristics of the received signal that are of interest. Second-order statistics, such as the complex autocorrelation function (ACF), which capture the evolution of the channel relative to time are also of significance. The complex ACF finds many uses in wireless channel modeling, such as the simulation of fading [39], [40] and the characterization of non-isotropic signal transmission and reception [40], [41].

In [42] the authors presented a unified model for short-term fading[1] in LoS, QLoS and NLoS signal propagation scenarios, referred to as the Three State Model (TSM). Within each state of this model, the dominant component can be perturbed by shadowing accompanied by a scattered signal contribution. As part of the study conducted in [42] the distribution of the in-phase and quadrature components and the distribution of the received signal envelope were derived. Building upon these contributions, in this paper we further develop the fundamental statistics of the TSM, obtaining expressions for the probability density functions (PDFs) of the received signal phase and the joint envelope-phase. We also further adapt the model to consider anisotropic filtering of the scattered signal contribution, which is accounted for through the TSM's second-order statistics, where the direction of departure (DoD) and DoA are modeled using the Von Mises distribution [41]. Movement of the TX, RX or both is also accounted for in the present work, leading to a novel formulation for the complex ACF of the TSM. It is worth mentioning that although at first glance, some of the expressions obtained for some of the fundamental statistics may appear arduous, a key feature of the TSM is that it is completely defined in terms of underlying Gaussian random variables (RVs), meaning that unlike many other comparable models, it has a strong physical motivation, and its simulation is relatively straightforward. Lastly, we provide an important demonstration of the utility of the TSM by fitting its newly developed statistics to data obtained from some field measurements taken in scenarios where transitions between channel states are likely to be encountered.

The remainder of this paper is organized as follows: The physical model underlying the TSM is described in Section II. In Section III, fundamental statistics of both the individual states and the TSM are obtained. Section IV firstly details the measurement setup, environment, and procedure. Afterwards the model fitting is presented for two example use cases. Lastly, Section V provides some concluding remarks.

II. Physical Model and Mathematical Formulation

The TSM characterizes scenarios where a fading channel may transition between three states, namely LoS, QLoS, or NLoS. Each state has an associated probability of occurrence, p_ι, such that $\sum_{\iota\in\{L,Q,N\}} p_\iota = 1$, where the elements in ι represent a state according to L = LoS, Q = QLoS, and N = NLoS. The transitions between the three states within the TSM can be modeled using a Markov process. The transition from one state to the next corresponds to a change in the state of the (direct) optical signal path between the TX and RX. As depicted in the state-transition-rate diagram of Fig. 1, the transition rate from the LoS state to the QLoS state and back again is β_0 and ν_1, respectively. Likewise, the transition rate from the QLoS state to the NLoS state and back is β_1 and ν_2, respectively. Following from this, we may define the ratios, $A_0 = \beta_0/\nu_1$ and $A_1 = \beta_1/\nu_2$, with both A_0 and A_1 being positive real numbers. This then allows us to write the probability of occurrence of each of the three states as [43]

[1]Or equivalently small-scale fading if considering distance instead of time.

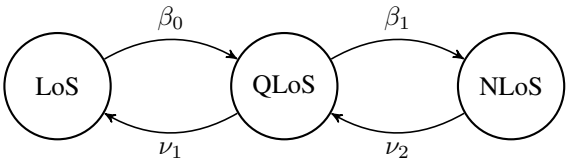

Fig. 1: The state-transition-rate diagram of the TSM.

$$p_L = [1 + A_0 + A_0 A_1]^{-1}, \tag{1}$$
$$p_Q = p_L A_0, \tag{2}$$
$$p_N = p_L A_0 A_1. \tag{3}$$

In addition to these mathematical relationships between the transition rates and steady state probabilities, it is convenient to establish some qualitative links between them. Letting S_0, S_1 and S_2 represent the LoS, QLoS, and NLoS respectively, then for $A_i = 1$, the states S_i and S_{i+1} are equally likely. For $A_i > 1$, S_{i+1} is more likely than S_i, and otherwise for $A_i < 1$. The QLoS state can be interpreted as a transitionary state, where the geometry, and hence statistics of the channel are not fully described by either LoS or NLoS.

Since only one of the three states may occur at a time, $\mathcal{S} = R_\iota \exp(j\Theta_\iota)$ represents the complex signal envelope at a particular instance, where R_ι is the received signal envelope and Θ_ι is the phase of an individual state. In many signal propagation scenarios, especially in short range applications the geometry of the propagation problem is such that dominant signal paths may exist even in what would be considered a NLoS channel (e.g., via a strong specular reflection from a smooth wall or similar surface). In such scenarios, any dominant component which may be present could be subjected to shadowing. Any shadowing affecting the dominant component in each state is described through an independent shadowing process, causing the dominant component to fluctuate. Letting X_ι and Y_ι represent the in-phase and quadrature components of a state respectively, it follows that,

$$\mathcal{S} = X_\iota + jY_\iota, \tag{4}$$
$$R_\iota^2 = X_\iota^2 + Y_\iota^2, \tag{5}$$
$$\Theta_\iota = \arg(X_\iota + jY_\iota), \tag{6}$$
$$X_\iota = R_\iota \cos(\Theta_\iota), \tag{7}$$
$$Y_\iota = R_\iota \sin(\Theta_\iota). \tag{8}$$

The received signal power of each state, can then be modeled as

$$R_\iota^2 = (C_{sca-i,\iota} + \zeta_\iota C_{dom-i,\iota})^2 + (C_{sca-q,\iota} + \zeta_\iota C_{dom-q,\iota})^2, \tag{9}$$

where $C_{sca-i,\iota}$ and $C_{sca-q,\iota}$ are mutually independent Gaussian random processes with $\mathbb{E}[C_{sca-i,\iota}] = \mathbb{E}[C_{sca-q,\iota}] = 0$, $\mathbb{E}[C_{sca-i,\iota}^2] = \mathbb{E}[C_{sca-q,\iota}^2] = \sigma_\iota^2$, where $\mathbb{E}[\cdot]$ denotes statistical expectation. $C_{dom-i,\iota}$ and $C_{dom-q,\iota}$ represent the time-varying amplitudes of the in-phase and quadrature components of the dominant signal respectively, with the variation related to the embedded Doppler effect [44], and ζ_ι models the fluctuations of the dominant component. The Rician k factor of each state represents the ratio between the total power of the dominant component, $\delta_\iota^2 = C_{dom-i,\iota}^2 + C_{dom-q,\iota}^2$, and the total power of the scattered components $2\sigma_\iota^2$, with

$$2\sigma_\iota^2 = \frac{\bar{r}_\iota^2}{(1 + k_\iota)}, \tag{10}$$

where $\bar{r}_\iota = \sqrt{\mathbb{E}[R_\iota^2]}$, that is,

$$k_\iota = \frac{C_{dom-i,\iota}^2 + C_{dom-q,\iota}^2}{2\sigma_\iota^2}. \tag{11}$$

By defining

$$\varpi_\iota = \arg(C_{dom-i,\iota} + jC_{dom-q,\iota}) \tag{12}$$

as a phase parameter, we can write

$$C_{dom-i,\iota} = \sqrt{\frac{k_\iota}{1 + k_\iota}} \bar{r}_\iota \cos(\varpi_\iota), \tag{13}$$
$$C_{dom-q,\iota} = \sqrt{\frac{k_\iota}{1 + k_\iota}} \bar{r}_\iota \sin(\varpi_\iota). \tag{14}$$

The normalized term, ζ_ι, simultaneously impacts both the in-phase and quadrature components. It accounts for any fluctuations of the dominant component in each individual state caused by shadowing, and follows a normalized Rician distribution with PDF given by [45, eq. (2.62)] (substituting $\Omega_p = 1$)

$$f_{\zeta_\iota}(\zeta_\iota) = \frac{2\zeta_\iota (1 + k_{S_\iota}) \exp(-k_{S_\iota})}{\exp(\zeta_\iota^2 (1 + k_{S_\iota}))} I_0\left(2\zeta_\iota \sqrt{k_{S_\iota}(1 + k_{S_\iota})}\right), \tag{15}$$

where $I_0(\cdot)$ denotes the modified Bessel function of the first kind with order zero [46, eq. (8.447.1)] and $\mathbb{E}[\zeta_\iota^2] = 1$. The parameter k_{S_ι} controls the severity of the shadowing of the dominant component, with $k_{S_\iota} \to 0$, indicating severe shadowing whereas the shadowing vanishes as $k_{S_\iota} \to \infty$. The Nakagami-*m* distribution has been used as an alternative to the lognormal distribution to model shadowing of the dominant component [38]. In this work, we use the Rician distribution to approximate the Nakagami-*m* distribution [45], although it is worth highlighting that the Rician distribution has previously been used in its own right to model shadowing in indoor scenarios [47].

III. Distribution of the Quadrature Components, Received Signal Envelope, Received Signal Phase and the Complex ACF

Utilizing the physical model defined above, the distribution of the in-phase and quadrature components of the complex received signal, the distribution of the received signal envelope, the distribution of the received signal phase, and the complex ACF are now obtained.

A. Distribution of the In-phase and Quadrature Components

Let either

$$Z_\iota = X_\iota \ \& \ \lambda_\iota = C_{dom-i,\iota} \tag{16}$$

or

$$Z_\iota = Y_\iota \ \& \ \lambda_\iota = C_{dom-q,\iota} \tag{17}$$

as required to represent either the in-phase or quadrature components of the complex received signal, respectively. For brevity the derivation for the distribution of the in-phase and quadrature components is omitted here but it is included in Appendix A, along with a closed-form solution. The PDF of the in-phase or quadrature components for each of the individual states is shown in (19), where

$$\eta_\iota = \bar{r}_\iota^2(1+k_{S\iota}) + \lambda_\iota^2(1+k_\iota), \tag{18}$$

$\Gamma(\cdot)$ is the gamma function [48, eq. (06.05.02.0001.01)], and ${}_1F_1(\cdot;\cdot;\cdot)$ is the confluent hypergeometric function [46, eq. (9.210.1)].

From the physical model of the TSM it is clear that the associated TSM first-order statistics are a combination of the three individual state first-order statistics in proportion with their probability of occurrence (i.e., p_L, p_Q and p_N). Now letting $\bar{r}_g = \sqrt{\mathbb{E}[R^2]}$, where

$$\bar{r}_g = \sum_{\iota\in\{L,Q,N\}} p_\iota \bar{r}_\iota \tag{20}$$

and using a transformation of variables ($z_\iota = z/\bar{r}_g$) the PDF of the in-phase or quadrature components of the TSM can be found as

$$f_Z(z) = \bar{r}_g \sum_{\iota\in\{L,Q,N\}} p_\iota f_{Z_\iota}(z \times \bar{r}_g), \tag{21}$$

where $f_{Z_\iota}(\cdot)$ denotes the PDF of the in-phase or quadrature components for the relevant state as presented in (19). The PDFs of the in-phase and quadrature component are re-normalized to $\bar{r}_g$, the overall rms signal level, to ensure Z has unit power. In order to corroborate our new expressions, Monte Carlo simulations have been carried out by generating 10^7 samples of each of the underlying random processes, $C_{sca-i,\iota}$, $C_{sca-q,\iota}$, and ζ_ι and evaluating (9). Fig. 2 provides plots of the theoretical PDFs of the in-phase and quadrature components along with respective results of simulations for an example TSM fading scenario. It should be noted that for all examples presented in this section, the transition ratios A_0 and A_1, have been conveniently chosen to yield specific values of p_L, p_Q and p_N. For illustrative purposes, ϖ is considered to be time-invariant for all examples presented in this section. In this example the LoS state occurs most often with $p_L = 0.4$, a strong dominant component exists such that $k_L = 15$, which suffers from negligible shadowing characterized by $k_{SL} = 10$, and $\varpi_L = \pi/2$ rad. The QLoS state occurs between that of the LoS and NLoS states with a probability of $p_Q = 0.3$, it has a weaker dominant component compared to the LoS state with $k_Q = 5$, moderate shadowing with, $k_{SQ} = 1$, and $\varpi_Q = -\pi/2$ rad. Lastly the NLoS state has a probability of occurrence of $p_N = 0.3$, a weak dominant component exists that suffers severe shadowing resulting in $k_N = 0.2$, $k_{SN} = 0.15$, and $\varpi_N = 0$ rad. It is also noted that for all states $\bar{r}_\iota = 1$. The figure shows that the PDFs of the in-phase and quadrature components of the complex received signal of the TSM can be vastly different even when experiencing the same fading conditions. For instance, the in-phase component appears to be unimodal, whilst the quadrature component is not.

B. Distribution of the Received Signal Envelope

For brevity the derivation of the PDF of the received signal envelope in each state, R_ι, is omitted here, the proof and a closed-form solution is provided in Appendix B. The PDF of the received signal envelope in each state, R_ι, is found to be

$$\begin{aligned} f_{R_\iota}(r_\iota) = \sum_{i=0}^{\infty} & \frac{2r_\iota^{1+2i} k_\iota^i (1+k_\iota)^{1+i} \mu_\iota \exp(-k_{S\iota})}{i!\bar{r}_\iota^{2(1+i)}(1+k_\iota+k_{S\iota})^i} \\ & \times \exp\left(-\frac{r_\iota^2(1+k_\iota)}{\bar{r}_\iota^2}\right) {}_1F_1\Big(1+i;1;k_{S\iota}\mu_\iota\Big), \end{aligned} \tag{22}$$

where

$$\mu_\iota = (1+k_{S\iota}) / (1+k_\iota+k_{S\iota}). \tag{23}$$

As $k_{S\iota} \to \infty$, (i.e., as the impact of shadowing on the dominant components vanishes), the PDF given in (22) approaches that of the Rician distribution. Secondly, when $k_{S\iota} \to 0$ or $k_\iota = 0$, (22) reduces to the Rayleigh PDF.

Using a transformation of variables ($r_\iota = r/\bar{r}_g$), the PDF of the received signal envelope of the TSM is shown to be

$$f_R(r) = \bar{r}_g \sum_{\iota\in\{L,Q,N\}} p_\iota f_{R_\iota}(r \times \bar{r}_g), \tag{24}$$

where $f_{R_\iota}(\cdot)$ represents the PDF of the received signal envelope for each of the individual states as given in (22). The PDF of the received signal envelope is re-normalized to the overall rms signal level to ensure R has unit power. The effect p_ι has on the PDF of the TSM received signal envelope is now examined in Fig. 3, using the same fading conditions which provided the results in Fig. 2 with p_ι now varying. In this example, the LoS state resembles Rician fading due to the strong dominant component and the weak shadowing, whilst the NLoS state resembles Rayleigh fading.

C. Distribution of the Received Signal Phase

It is recalled that in order to determine the distribution of the received signal phase, the joint distribution of the envelope and phase must be found. Aside from being an intermediate step in the determination of the PDF of the signal phase, the joint distribution of the envelope and phase has independent value, as it may be used to determine higher order statistics for single or multi-branch diversity systems [49]. The joint distribution of the envelope and phase of each state is provided in (25), where

$$\Delta_\iota(\theta_\iota, \varpi_\iota) = \frac{k_\iota \cos^2(\theta_\iota - \varpi_\iota)}{1+k_\iota+k_{S\iota}}. \tag{27}$$

The derivation of the joint distribution of the envelope and phase of each state is presented in Appendix C, along with a closed-form solution.

By integrating the PDF of the joint envelope-phase in (25) with respect to the received signal envelope, R_ι, the PDF of the signal phase is obtained as shown in (26), where ${}_2F_1(\cdot,\cdot;\cdot;\cdot)$ denotes the Gauss hypergeometric function [46, eq. (9.100)]. The accompanying derivation and closed-form solution is provided in Appendix D. Following from this, the PDF of the signal phase of the TSM can now be written as

$$f_\Theta(\theta) = \sum_{\iota\in\{L,Q,N\}} p_\iota f_{\Theta_\iota}(\theta), \tag{28}$$

where $f_{\Theta_\iota}(\cdot)$ is the PDF of the signal phase for the individual states as given in (26). Next, the effect ϖ_ι has on the TSM received signal phase is examined by using the same fading conditions as the ones in Fig. 2 but with ϖ_ι now varying. From Fig. 4 it can be observed that the PDF of the signal phase is multimodal, with different peaks (local maxima) at $\theta_\iota = \varpi_\iota$ corresponding to the different states, whereas the minima are

$$f_{Z_\iota}(z_\iota) = \sum_{i=0}^{\infty} \frac{\sqrt{1+k_\iota}\,(1+k_{S_\iota})^{1+i}\, k_{S_\iota}^{i} \bar{r}_\iota^{2i} \exp\left(-k_{S_\iota}\right)}{\sqrt{\pi}\eta_\iota^{\frac{3}{2}+i}\Gamma(1+i) i! \exp\left(\frac{z_\iota^2(1+k_\iota)}{\bar{r}_\iota^2}\right)} \left[\bar{r}_\iota \Gamma\left(1+i\right) \sqrt{\eta_\iota} {}_1F_1\left(1+i; \frac{1}{2}; \frac{\left(z_\iota \lambda_\iota (1+k_\iota)\right)^2}{\bar{r}_\iota^2 \eta_\iota}\right) \right.$$
$$\left. + 2 z_\iota \lambda_\iota (1+k_\iota) \Gamma\left(\frac{3}{2}+i\right) {}_1F_1\left(\frac{3}{2}+i; \frac{3}{2}; \frac{\left(z_\iota \lambda_\iota (1+k_\iota)\right)^2}{\bar{r}_\iota^2 \eta_\iota}\right) \right]. \tag{19}$$

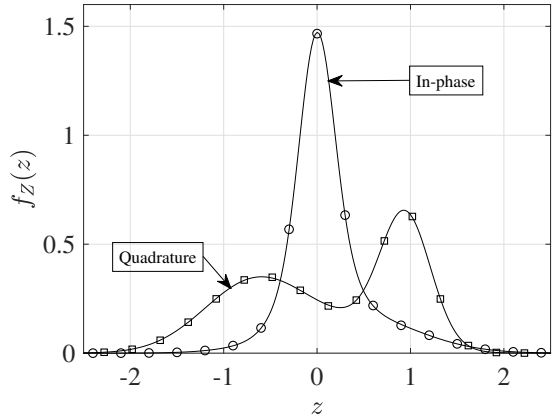

Fig. 2: The in-phase and quadrature PDFs of the TSM (lines) and corresponding simulation results (shapes).

localized at $\theta_\iota = \varpi_\iota + \pi$. However, if ϖ_ι is similar across all three states, the PDF of the TSM received signal phase will appear to be unimodal. From Figs. 2, 3 and 4, it is worth highlighting that the analyzed statistical distributions show quite distinct behaviors, under the same fading conditions. While the in-phase, quadrature components, and the signal phase can clearly be characterized by a multimodal PDF, such multimodal behavior may not be as distinctive or even occur in the received signal envelope. This is an important observation that will have implications for wireless system models that use extrapolations of so-called 'amplitude only' fading to define in-phase, quadrature and phase characteristics. Importantly, the above observation is also noticed to occur in one of the example applications presented in the sequel demonstrating that it is also a real-world physical phenomena.

D. Complex Autocorrelation Function

Unlike the first-order statistics, the ACF shows how channel observations change over time. To this effect and since the TSM is composed of three states that occur individually, we now examine the ACF of the TSM when the complex received signal, which is assumed to be wide sense stationary, is in any one of the described states for any period of time. The autocorrelation of a wide sense stationary process may be written as $\phi_{\mathcal{SS}}(\tau) = \mathbb{E}\left[\mathcal{S}(t)\mathcal{S}^*(t+\tau)\right]$, where $\mathcal{S}$ is the complex received signal whilst the TSM is in a particular state, t is the current time and τ is the time lag [45]. Using the model given in (9) for the complex received signal of the individual states and after some mathematical manipulation, the autocorrelation may be expressed as

$$\phi_{\mathcal{SS}}(\tau) = \frac{\bar{r}_\iota^2}{1+k_\iota} \mathbb{E}\big[\varrho_\iota(t)\varrho_\iota^*(t+\tau) + k_\iota \zeta_\iota(t)\zeta_\iota(t+\tau) \times \delta_\iota(t)\delta_\iota^*(t+\tau)\big], \tag{29}$$

where $\varrho_\iota(t)$ represents the amplitude of the complex received signal due to the scattered component of the individual state, $\delta_\iota(t)$ represents the dominant signal component, and $\zeta_\iota(t)$ is the corresponding Rician shadowing process.

1) Autocorrelation of the Dominant Signal Component and Shadowing: By introducing the concept of relative motion [50], the dominant signal component in each individual state, $\delta_\iota(t)$, is expressed as $\exp\left(j\left(2\pi f_{\delta_\iota} t \cos\left(\alpha_{\delta_\iota}\right) + \varphi_{0_\iota}\right)\right)$, where f_{δ_ι} is the relative Doppler frequency, and α_{δ_ι} is the DoA of the dominant component at the receiver [41], [51]. In this model, φ_{0_ι} is the initial phase, uniformly distributed on the interval $[-\pi, \pi]$. This results in

$$\mathbb{E}[\delta_\iota(t)\delta_\iota^*(t+\tau)] = \exp\left(j2\pi f_{\delta_\iota}\tau\cos\left(\alpha_{\delta_\iota}\right)\right). \tag{30}$$

The shadowing process that causes the dominant signal component to fluctuate is represented by a normalized random process, $\zeta_\iota(t)$, with PDF given in (15). The ACF of a normalized Rician random process is known as [52, eq. (12)]. Using this, the ACF of the shadowing in each state, $\mathbb{E}[\zeta_\iota(t)\zeta_\iota(t+\tau)]$, is obtained as

$$\phi_{\zeta_\iota\zeta_\iota}(\tau) = \frac{\pi}{4} {}_2F_1\left(-\frac{1}{2}, -\frac{1}{2}; 1; \left(\frac{J_0(2\pi f_{S_\iota}\tau) + k_{S_\iota}}{1+k_{S_\iota}}\right)^2\right), \tag{31}$$

where $J_0(\cdot)$ is the zeroth-order Bessel function of the first kind [46, eq. (8.441.1)] and f_{S_ι} represents the maximum Doppler frequency induced by shadowing. It should be noted that we have adopted the model given in [53] to successfully characterize the autocorrelation of the shadowing process. This is not prescriptive and is one of a number of plausible autocorrelation functions that could be used to capture the time correlation properties of the LoS shadowing.

2) Autocorrelation of the Scattered Signal Component: Using Akki and Haber's model [54] to represent the scattered signal components and the notation in [45, p. 82], the amplitude of the scattered component of the normalized flat fading complex received signal for each of the individual states can be written as

$$\varrho_\iota(t) = \sqrt{\frac{1}{\mathcal{Q}}} \sum_{q=1}^{\mathcal{Q}} \exp\left(j2\pi t f_{T_\iota}\cos\left(\alpha_{q,T_\iota}\right)\right) \times \exp\left(j2\pi t f_{R_\iota}\cos\left(\alpha_{q,R_\iota}\right) + j\varphi_{q_\iota}\right), \tag{32}$$

where $\mathcal{Q}$ is the number of propagation paths, f_{T_ι} and f_{R_ι} are the maximum Doppler frequencies at the TX and RX respectively, α_{q,T_ι} is the random DoD and α_{q,R_ι} is the random DoA, of the q^{th} propagation path with reference to the TX and RX velocity vectors respectively. The variable φ_{q_ι} is a random

$$f_{R_\iota,\Theta_\iota}(r_\iota,\theta_\iota)=\sum_{i=0}^{\infty}\frac{r_\iota(1+k_\iota)\mu_\iota^{1+i}k_{S_\iota}^{i}\exp\left(-\frac{r_\iota^2(1+k_\iota)}{\bar{r}_\iota^2}\right)}{\pi\bar{r}_\iota^2\Gamma(1+i)i!\exp\left(k_{S_\iota}\right)}\left[\Gamma(1+i){}_1F_1\left(1+i,\frac{1}{2};\frac{r_\iota^2(1+k_\iota)\Delta_\iota(\theta_\iota,\varpi_\iota)}{\bar{r}_\iota^2}\right)\right.$$
$$\left.+\frac{r_\iota}{\bar{r}_\iota}2\sqrt{1+k_\iota}\Gamma\left(\frac{3}{2}+i\right)\sqrt{\Delta_\iota(\theta_\iota,\varpi_\iota)}{}_1F_1\left(\frac{3}{2}+i,\frac{3}{2};\frac{r_\iota^2(1+k_\iota)\Delta_\iota(\theta_\iota,\varpi_\iota)}{\bar{r}_\iota^2}\right)\right]. \tag{25}$$

$$f_{\Theta_\iota}(\theta_\iota)=\sum_{i=0}^{\infty}\frac{\mu_\iota\exp\left(-k_{S\iota}\right)\left(k_{S\iota}\mu_\iota\right)^i}{2\pi\Gamma(1+i)i!}\left[\Gamma(1+i){}_2F_1\left(1,1+i;\frac{1}{2};\Delta_\iota(\theta_\iota,\varpi_\iota)\right)\right.$$
$$\left.+\Gamma\left(\frac{3}{2}+i\right)\sqrt{\pi\Delta_\iota(\theta_\iota,\varpi_\iota)}{}_2F_1\left(\frac{3}{2}+i,\frac{3}{2};\frac{3}{2};\Delta_\iota(\theta_\iota,\varpi_\iota)\right)\right]. \tag{26}$$

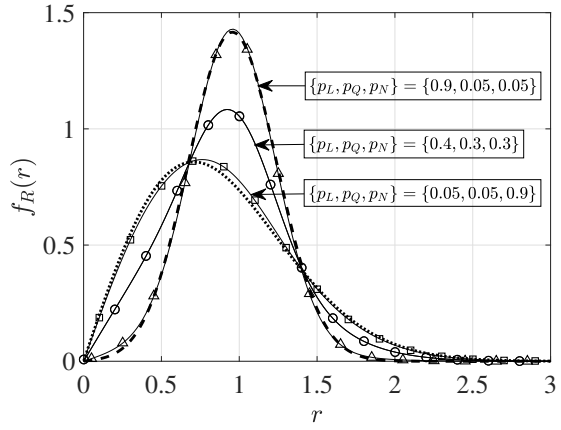

Fig. 3: The PDF of the TSM received signal envelope (lines) and corresponding simulation results (shapes) are shown for p_ι varying. The Rician PDF (dashed line) is shown for $K=5$, $\bar{r}=1$, and the Rayleigh PDF (dotted line) is shown for $\bar{r}=1$.

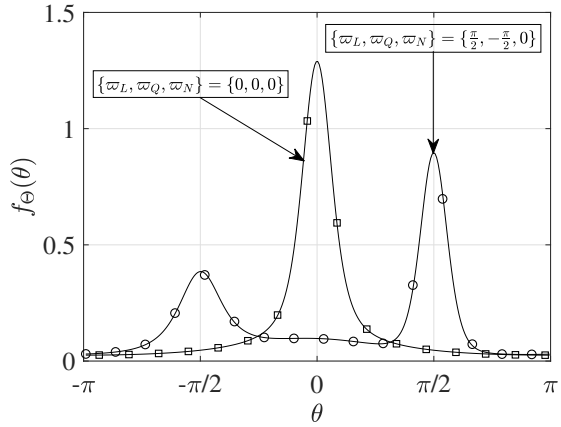

Fig. 4: The PDF of the TSM received signal phase (lines) and corresponding simulation results (shapes) for varying ϖ_ι (rad).

phase uniformly distributed on $[-\pi,\pi]$ and is independent of α_{q,T_ι} and α_{q,R_ι} for all q.

The distribution of the DoD or DoA of the scattered signal component can be modeled using the versatile Von Mises PDF [41]. This distribution can be used to model realistic fading scenarios in which DoD or DoA of multipath waves are either isotropic or non-isotropic. The Von Mises PDF for the DoD (or DoA) of the scattered signal contribution in each individual state, $f_{\mathcal{A}_\iota}(\alpha_\iota)$, is given by [41]

$$f_{\mathcal{A}_\iota}(\alpha_\iota)=\frac{\exp\left(\kappa_\iota\cos\left(\alpha_\iota-\bar{\alpha}_\iota\right)\right)}{2\pi I_0(\kappa_\iota)}, \tag{33}$$

where $\alpha_\iota\in[-\pi,\pi]$, $\kappa_\iota\geq 0$ controls the spread of the DoD (κ_{T_ι}) and the DoA (κ_{R_ι}). The mean DoD and DoA are accounted for by $\bar{\alpha}_{T_\iota}$ and $\bar{\alpha}_{R_\iota}$, respectively, and each can have values in the range $[-\pi,\pi]$. When $\kappa_\iota=0$, (33) reduces to the circular uniform distribution and the experienced fading is described by isotropic scattering. As κ_ι increases, the DoD or DoA becomes increasingly unidirectional with $\kappa_\iota\to\infty$ describing extremely non-isotropic scattering. As discussed in [41], a useful estimator of the spread of the DoD or DoA in polar coordinates for increasing values of κ_ι (i.e., $\kappa_\iota>1$) can be obtained by considering the inflexion points of $f_{\mathcal{A}_\iota}(\alpha_\iota)$ which are approximately equal to $\pm1/\sqrt{\kappa_\iota}$. For highly non-isotropic scattering, e.g., for $\kappa_\iota=3$ and 5, the spread of the DoD or DoA of these contributions can be estimated as $2/\sqrt{\kappa_\iota}$, giving 66° and 51° respectively.

Now the autocorrelation of the scattered component is evaluated, i.e., $\mathbb{E}\left[\varrho_\iota(t)\varrho_\iota^*(t+\tau)\right]$. To this end, assuming the number of propagation paths is infinite, and after some algebraic manipulations, we obtain

$$\phi_{\varrho_\iota\varrho_\iota}(\tau)=\lim_{\mathcal{Q}\to\infty}\sqrt{\frac{1}{\mathcal{Q}}}\sum_{q=1}^{\mathcal{Q}}\mathbb{E}\big[\exp\left(j2\pi f_{T_\iota}\tau\cos\left(\alpha_{q,T_\iota}\right)\right)$$
$$\times\exp\left(j2\pi f_{R_\iota}\tau\cos\left(\alpha_{q,R_\iota}\right)\right)\big]. \tag{34}$$

Knowing that α_{T_ι} and α_{R_ι} are independent RVs and using the PDF in (33) along with [46, eq. (3.338.4)], yields (35).

3) Autocorrelation Function: Using (30), (31) and (35) in (29), we obtain the ACF for an individual TSM state, given in (36). The ACF is expressed in closed-form and it is general for both isotropic (i.e., $\kappa_{T_\iota}=\kappa_{R_\iota}=0$) and non-isotropic (i.e., κ_{T_ι} or $\kappa_{R_\iota}>0$) fading conditions. For convenience, the ACF in its normalized form, $\tilde{\phi}_{SS}(\tau)$, is found by setting $\bar{r}_\iota=1$. A summary of the parameters used in the TSM and their description is given in Table I.

Fig. 5 shows example plots of the normalized complex ACF (i.e., $\bar{r}_\iota=1$), when the RX is stationary (i.e., $f_{R_\iota}=0$ Hz) and the TX is in motion (i.e., $f_{T_\iota}=10$ Hz). The simulated

$$\phi_{\varrho_\iota\varrho_\iota}(\tau) = \frac{I_0\left(\sqrt{\kappa_{T_\iota}^2 - 4\pi^2 f_{T_\iota}^2\tau^2 + j4\pi\kappa_{T_\iota}\cos(\bar{\alpha}_{T_\iota})f_{T_\iota}\tau}\right)}{I_0(\kappa_{T_\iota})} \frac{I_0\left(\sqrt{\kappa_{R_\iota}^2 - 4\pi^2 f_{R_\iota}^2\tau^2 + j4\pi\kappa_{R_\iota}\cos(\bar{\alpha}_{R_\iota})f_{R_\iota}\tau}\right)}{I_0(\kappa_{R_\iota})}. \tag{35}$$

$$\begin{aligned}\phi_{\mathcal{SS}}(\tau) = \frac{\bar{r}_\iota^2}{1+k_\iota}\Bigg[&\frac{I_0\left(\sqrt{\kappa_{T_\iota}^2 - 4\pi^2 f_{T_\iota}^2\tau^2 + j4\pi\kappa_{T_\iota}\cos(\bar{\alpha}_{T_\iota})f_{T_\iota}\tau}\right)}{I_0(\kappa_{T_\iota})} \frac{I_0\left(\sqrt{\kappa_{R_\iota}^2 - 4\pi^2 f_{R_\iota}^2\tau^2 + j4\pi\kappa_{R_\iota}\cos(\bar{\alpha}_{R_\iota})f_{R_\iota}\tau}\right)}{I_0(\kappa_{R_\iota})} \\ &+ \frac{k_\iota\pi}{4}{}_2F_1\left(-\frac{1}{2},-\frac{1}{2};1;\left(\frac{J_0(2\pi f_{S_\iota}\tau)+k_{S_\iota}}{1+k_{S_\iota}}\right)^2\right)\exp\left(j2\pi f_{\delta_\iota}\tau\cos(\alpha_{\delta_\iota})\right)\Bigg].\end{aligned} \tag{36}$$

results in Fig. 5 were obtained using the autoregressive (AR) simulation method described in [39] to generate 1×10^6 samples, using a model order of 200, and a bias of 1×10^{-9} to condition the Yule-Walker equations. The shadowing process that causes the dominant signal component to fluctuate and the other signal components were generated separately using AR modeling and then combined as detailed in (9).

The real part of the ACF in Fig. 5(a) shows a stronger correlation in the presence of a strong dominant component, i.e., Rician fading ($k_\iota = 3$ and $k_{S_\iota} = \infty$), as compared to the case where the dominant component is weak, i.e., Rayleigh fading ($k_\iota = 0$ and $k_{S_\iota} = \infty$). When shadowing of the dominant component is present (i.e., $k_{S_\iota} = 0.5$), the autocorrelation function is found in the region between those obtained for the Rayleigh and Rician cases, as expected. Comparing the real part in Fig. 5(a) to the imaginary part in Fig. 5(b), which is a measure of the cross-correlation of the real and imaginary parts of the complex received signal [45], we observe that shadowing has no effect on the cross-correlation of the two quadrature components in this particular example, since $f_{\delta_\iota} = 0$ Hz. The effect of increasing f_{S_ι} upon the autocorrelation of the signal is also depicted in Fig. 5. Holding k_{S_ι} constant (i.e., $k_{S_\iota} = 0.5$), as f_{S_ι} increases the dominant component correlates and decorrelates more rapidly. This reflects the increased temporal variation in the channel and results in a more irregular (less smooth) ACF.

IV. Two Example Use Cases

In this section, the TSM is used to fit field measurements for two realistic wireless communication applications which are known to be subject to LoS, QLoS and NLoS channel states, namely off-body communications for a rotating user and off-body communications with a pedestrian intersecting the direct signal path between the TX and RX.

A. Experimental setup

The measurements were conducted in the first-floor seminar room of the ECIT building at Queen's University Belfast in the United Kingdom (see [55] for a more detailed description of the measurement environment). In both experiments, the TX and RX used the patch antenna described in [56]. The antennas were connected to a Rhode & Schwarz ZVB-8 vector network analyzer (VNA) using calibrated low loss coaxial cables. The VNA was set to record snapshots of the complex S_{21} every 2 ms at 2.45 GHz using a 10 kHz resolution bandwidth. The duration of the measurements for the rotating user and pedestrian crossing the LoS signal path experiments were 30 s and 10 s respectively. For both example use cases, the TX antenna was mounted vertically on a nonconductive height adjustable stand at an elevation of 1.40 m above the floor level, while the RX antenna was attached with its ground plane parallel to a phantom representative of human muscle tissue as used in [57], at the same height as the TX antenna.

To obtain the first-order parameter estimates, the theoretical PDFs given in equations (21), (24), and (28) were fitted to the entire complex S_{21} data set collected for each experiment. The complex S_{21} data was normalized to the empirical global rms signal level, before using a non-linear least squares routine, programed in MATLAB to fit the equations. Following from this, the estimated parameters were used to label each of the individual states (i.e., LoS, QLoS and NLoS) and subsequently to fit the complex ACF given in equation (36) for each of the three states. For simplicity during the fitting process and without loss of generality, we have considered ϖ to be constant. To obtain the parameter estimates for the second-order statistics, we extracted continuous segments of measurements of between 1 to 2 seconds in length from the LoS, QLoS and NLoS phases. The LoS, QLoS or NLoS channel states were identified from the video footage by interpreting the optical viewpoints of the TX and RX antennas. It is worth highlighting that we used the relevant parameter estimates for each state, obtained from the fitting of the first-order statistics (i.e., k_ι, k_{S_ι} and $\bar{r}_\iota$), to also fit the second-order statistics.

B. Rotating User

In this experiment, the RX antenna was attached to a human body phantom which was positioned on an electric rotating turntable (Isunking MT320RL32). As shown in Fig. 6(a), the RX antenna was initially oriented in direct optical LoS with the TX antenna at a distance of 9 m, and then rotated 180° clockwise such that direct optical LoS was obscured by the human body phantom. The turntable was programed to complete half a rotation in 30 s. Clearly, in this experiment, the channel between the TX and RX antennas was initially in a LoS state before changing to QLoS as the direct signal path became shadowed by the human body phantom, before finally arriving at the NLoS state where the phantom completely obscured the direct optical LoS path. This progression can be seen from the normalized received signal time series in Fig. 7, where the peak signal amplitude occurs at the beginning,

TABLE I: Summary of parameters in the TSM.

Parameter	Description	Values	Special Cases
k_ι	Ratio between the total power of the dominant signal component and the total power of the scattered signal components	$k_\iota \in [0, \infty)$	Rayleigh fading: $k_\iota = 0$
k_{S_ι}	Shadowing severity	$k_{S_\iota} \in [0, \infty)$	No shadowing: $k_{S_\iota} \to \infty$ Severe shadowing (i.e., Rayleigh fading): $k_{S_\iota} = 0$
ϖ_ι (rad)	Phase parameter	$\varpi_\iota \in [-\pi, \pi]$	$C_{dom-q,\iota} = 0$: $\varpi_\iota = 0, \pm\pi$ rad $C_{dom-i,\iota} = 0$: $\varpi_\iota = \pm\pi/2$ rad
$\bar{r}_\iota$	The state rms signal level	$\bar{r}_\iota \in (0, 2.5]$	Normalized ACF, $\tilde{\phi}_{\mathcal{SS}}(\tau)$: $\bar{r}_\iota = 1$
$\bar{r}_g$	The global rms signal level	$\bar{r}_g \in (0, 2.5]$	-
τ (s)	Time lag	$\tau \in \mathbb{R}_{\geq 0}$[1]	-
f_{S_ι} (Hz)	Maximum Doppler frequency of the shadowing	$f_{S_\iota} \in [0, \infty)$	No Doppler shift: $f_{S_\iota} = 0$ Hz
f_{δ_ι} (Hz)	Relative Doppler frequency of the dominant signal component	$f_{\delta_\iota} \in [0, \infty)$	No Doppler shift: $f_{\delta_\iota} = 0$ Hz
α_{δ_ι} (rad)	DoA of the dominant signal component	$\alpha_{\delta_\iota} \in [-\pi, \pi]$	-
κ_{T_ι}	Spread of the scattered signal from the transmitter	$\kappa_{T_\iota} \in [0, \infty)$	Isotropic: $\kappa_{T_\iota} = 0$
f_{T_ι} (Hz)	Maximum Doppler frequency of the TX	$f_{T_\iota} \in [0, \infty)$	No Doppler shift: $f_{T_\iota} = 0$ Hz
$\bar{\alpha}_{T_\iota}$ (rad)	Mean DoD of the transmitted scattered signal component	$\bar{\alpha}_{T_\iota} \in [-\pi, \pi]$	-
κ_{R_ι}	Spread of the scattered signal at the receiver	$\kappa_{R_\iota} \in [0, \infty)$	Isotropic: $\kappa_{R_\iota} = 0$
f_{R_ι} (Hz)	Maximum Doppler frequency of the RX	$f_{R_\iota} \in [0, \infty)$	No Doppler shift: $f_{R_\iota} = 0$ Hz
$\bar{\alpha}_{R_\iota}$ (rad)	Mean DoA of the received scattered signal component	$\bar{\alpha}_{R_\iota} \in [-\pi, \pi]$	-

[1] The notation $\mathbb{R}_{\geq 0}$ indicates the set of real numbers including zero.

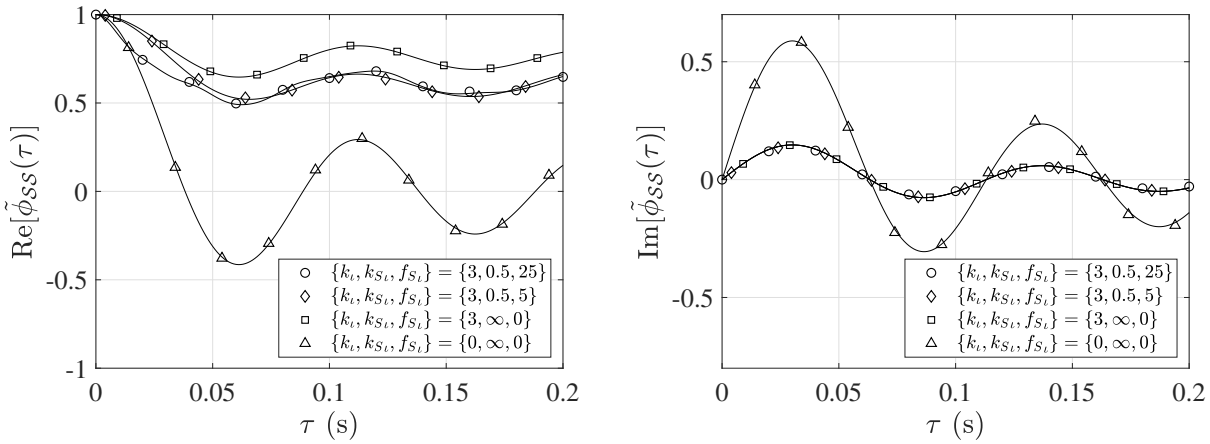

(a) Real part.

(b) Imaginary part.

Fig. 5: The normalized complex ACF (solid lines) in (36) and AR simulation results (shapes), with k_ι, k_{S_ι} and f_{S_ι} (Hz) varying using $\kappa_{T_\iota} = \kappa_{R_\iota} = 2$, $\bar{\alpha}_{T_\iota} = \bar{\alpha}_{R_\iota} = \pi/4$ rad, $f_{\delta_\iota} = 0$ Hz, $\alpha_{\delta_\iota} = 0$ rad, $f_{T_\iota} = 10$ Hz, $f_{R_\iota} = 0$ Hz.

followed by a transition through a series of lesser 'peaks' and nulls during the QLoS state before reaching the maximum optical NLoS condition.

In Table II and elsewhere, the $\hat{}$ operator is used to indicate a parameter estimate. Table II provides the parameter estimates of the first-order statistics for the best fit TSM for the rotating user measurement. The estimated power of the dominant and scattered signal components in each of the states is provided in Table III. From the results, it is apparent that a dominant signal component was always found to exist, even in the NLoS state where the direct optical LoS signal path was obscured by the phantom (i.e., $\hat{k}_\iota > 0$ and $\hat{\delta}^2_\iota > 0$). Nonetheless, it is clear there was a reduction in the power contributed by the dominant component transitioning from the LoS state, through QLoS, to the NLoS state. Interestingly, the power contributed through the scattered multipath remained consistent across all three states. These observations suggest that the dominant component became progressively shadowed and while the perceived DoD and DoA of the scattered signal contribution may have changed through the state transitions (see $\hat{\kappa}_{T_\iota}$ and $\hat{\kappa}_{R_\iota}$ in Table V), the overall power contributed to the received signal by this component was largely unchanged.

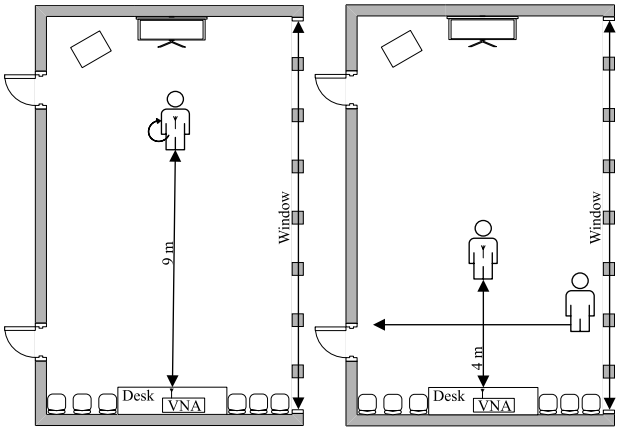

(a) The rotating user experiment. (b) The pedestrian crossing the LoS signal path experiment.

Fig. 6: Plan view of the measurement environment and experimental setups.

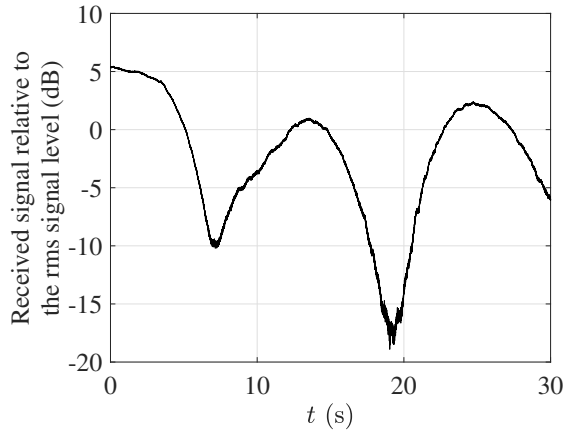

Fig. 7: Normalized received signal time series of the rotating user experiment.

TABLE II: TSM Parameter estimates for the fitted PDFs.

Experiment	ι	$\hat{p}_\iota$	$\hat{k}_\iota$	$\hat{k}_{S\iota}$	$\hat{\bar{r}}_\iota$	$\hat{\varpi}_\iota$ (rad)
Rotating user	L	0.09	17.34	37.75	1.51	-0.226π
	Q	0.32	5.85	0.86	0.86	-0.366π
	N	0.59	3.41	0.86	0.71	0.939π
Pedestrian crossing the LoS signal path	L	0.64	21.75	17.57	1.06	0.331π
	Q	0.11	12.69	39.89	0.92	-0.0223π
	N	0.25	12.93	2.58	0.76	0.395π

As anticipated the LoS state experienced the least perturbation caused by shadowing (i.e., $\hat{k}_{SL} = 37.75$) although as shown in Table II the LoS state was the least probable to be encountered as the phantom was rotated (i.e., $\hat{p}_L = 0.09$). Intuitively, the dominant components in both the QLoS and NLoS states suffered from shadowing of increased severity ($\hat{k}_{SQ} = 0.86$ and $\hat{k}_{SN} = 0.86$, respectively).

Fig. 8 shows the empirical probability densities of the measured in-phase and quadrature components, received signal envelope and received signal phase.[2] Also shown for comparison in Fig. 8 are the respective theoretical PDFs for each of the measures listed above. From Fig. 8 it can be seen that the proposed TSM provides a good fit to the empirical data. To assist with a numerical evaluation of the fits, the root mean square error (RMSE) of the theoretical PDF fits to the empirical data is given Table IV. Although not shown in Table IV, the RMSE of the Rician PDF (Fig. 8(c)) fitted to the empirical PDF of the received signal envelope obtained during the rotating user experiment was 4.65%, compared to that for the TSM which had an RMSE of 1.84% (Table IV). More importantly though, it provides a full characterization of the received signal, from its complex origin through to its amplitude and phase. From Figs. 8(a) and 8(b) it is clear that in the rotating user case, the underlying empirical in-phase and quadrature components have multiple modes caused by each of the three channel states (i.e., LoS, QLoS, and NLoS). It is worth mentioning that the modes of the theoretical PDFs coincide with the mean values of the in-phase and quadrature components, u_ι and v_ι, respectively, for each state, which can be calculated using the parameter estimates in Table II.

Although providing a good fit to the empirical probability densities of the in-phase and quadrature components, the TSM provided a less satisfactory fit to the empirical probability density of the received signal envelope (see Fig. 8(c)). In this case, although characterizing the lower and upper tails adequately, some digression was observed around the mode. The modality introduced by transitioning between the three states during the experiment can be seen in Fig. 8(d). Here the phase is clustered around a number of different phase levels (i.e., $\theta = 2.95$ rad and $\theta = -1$ rad). As we can see, despite the scattered signal contribution, the phase is very far from the uniform case as assumed in other multimodal models [31].

To examine the time correlation properties of the rotating user channel, two second excerpts of the normalized received

TABLE III: Estimated power of the dominant and scattered components.

Experiment	ι	$2\hat{\sigma}_\iota^2$	$\hat{\delta}_\iota^2$
Rotating User	L	0.12	2.17
	Q	0.11	0.63
	N	0.11	0.39
Pedestrian crossing the LoS signal path	L	0.05	1.07
	Q	0.06	0.77
	N	0.04	0.53

TABLE IV: RMSE (%) of the fitted PDFs.

Experiment	In-phase	Quadrature	Envelope	Phase
Rotating user	4.35	2.79	5.60	3.75
Pedestrian crossing the LoS signal path	2.69	3.39	1.84	3.82

[2]Note the empirical probability densities of the measured in-phase and quadrature components and the received signal envelope are normalized to the global rms signal level ($\bar{r}_g$).

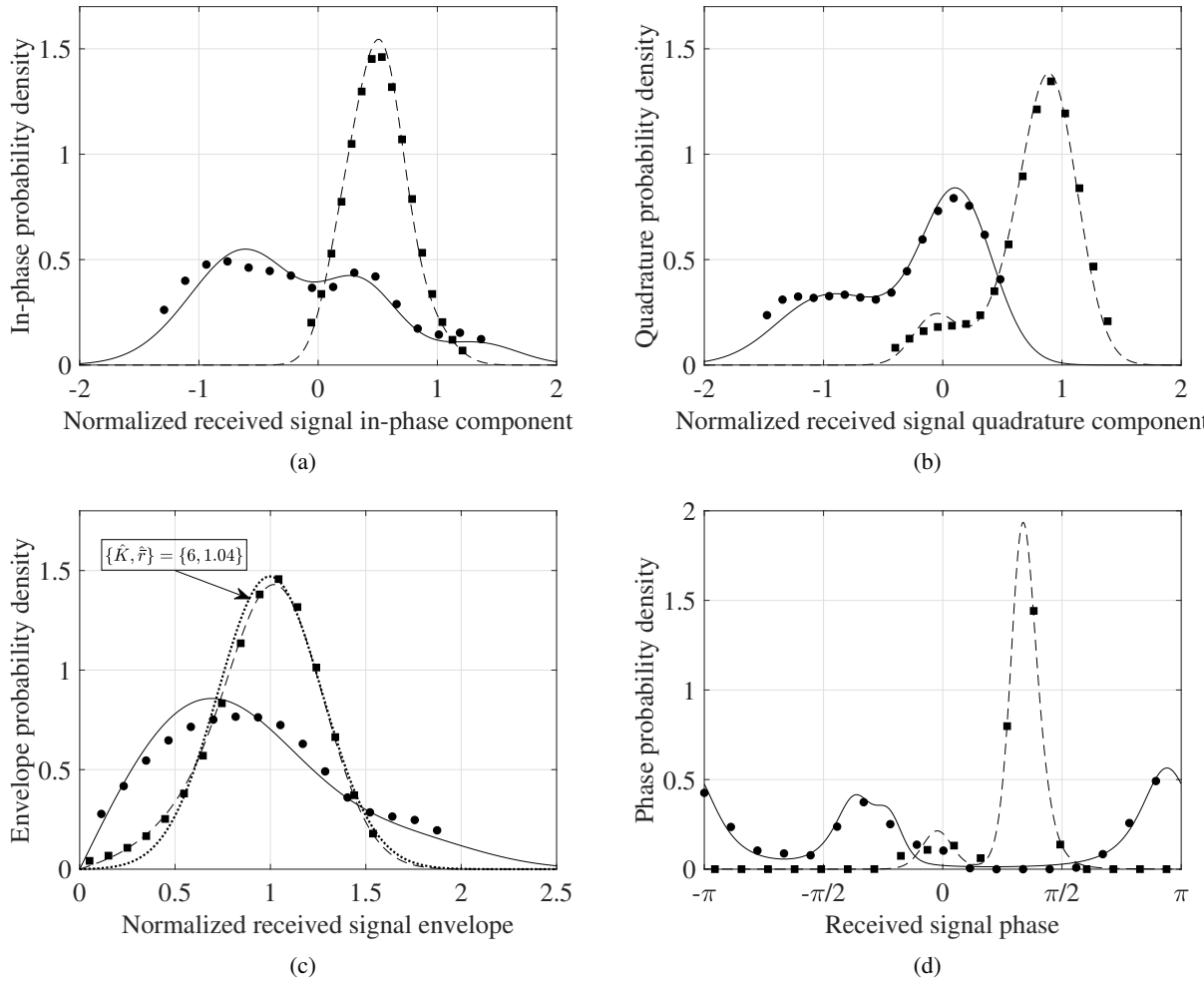

Fig. 8: The empirical and fitted theoretical TSM PDFs for the person crossing the LoS signal path and rotating user experiments. Note the empirical/theoretical PDFs for the person crossing the LoS signal path experiment are given by squares/dashed lines and the rotating user experiment by circles/solid lines, respectively. The Rician PDF fitted to the person crossing the LoS signal path experiment (dotted line) is also included in (c) for comparison.

signal for each state were examined. For the LoS state this was the first two seconds of the data. The corresponding intervals for the QLoS and NLoS channel states were 2 to 4 seconds and 28 to 30 seconds, respectively. All of the relevant parameter estimates for each state are given in Table V, with the exception of $\hat{k}_\iota$ and $\hat{k}_{S_\iota}$, which are already provided in Table II. Fig. 9 depicts the empirical complex autocorrelation function of the measurement data along side the theoretical ACF of the TSM model given in equation (36).[3] It can be observed that the TSM provides an excellent fit across all three states for both the real and imaginary parts of the empirical complex ACF. Over all three channel states, strong correlation was observed to persist in the real part of the complex ACF over the considered time window, with all three remaining above 0.88 (Fig. 9(a)). In contrast, the imaginary part of the complex ACF, which is a measure of the cross-correlation of the in-phase and quadrature components of the complex received signal, remained close to zero for all three states (Fig. 9(b)), suggesting that the two quadrature components are largely uncorrelated when considered over this duration.

C. Pedestrian Crossing the LoS Signal Path

The second example use case considered the scenario where a pedestrian intersected the optical LoS signal path in an off-body communications channel. For this set of measurements the TX and RX antennas were positioned in direct LoS as discussed above and separated from one another with a straight line distance of 4 m. An adult male of height 1.94 m and mass 110 kg acted as the pedestrian, and initially stood stationary at the window side of the room. They were then instructed to follow the trajectory annotated in Fig. 6(b), perpendicular to the optical LoS signal path between the antennas, such that they bisected the link. In this experiment, the channel between the TX and RX antennas was initially in a LoS state, before changing to QLoS as the pedestrian approached the off-body link, before entering the NLoS state as they blocked the direct signal path entirely. Afterwards the channel returned to the QLoS state and finally the LoS state when the

[3]It should be noted that all of the correlation functions in Fig. 9 have been normalized, i.e., $\bar{r}_\iota = 1$.

TABLE V: Parameter estimate for the fitted complex ACFs of each state.

Experiment	ι	$\hat{f}_{S_\iota}$ (Hz)	$\hat{f}_{\delta_\iota}$ (Hz)	$\hat{\alpha}_{\delta_\iota}$ (rad)	$\hat{\kappa}_{T_\iota}$	$\hat{f}_{T_\iota}$ (Hz)	$\hat{\bar{\alpha}}_{T_\iota}$ (rad)	$\hat{\kappa}_{R_\iota}$	$\hat{f}_{R_\iota}$ (Hz)	$\hat{\bar{\alpha}}_{R_\iota}$ (rad)
Rotating user	L	8.71	0.47	0.507π	20	0.01	-0.997π	0	3.03	0
	Q	0.26	1.72	-0.503π	2.95	4.86	-0.994π	3.19	4.72	0
	N	0	0.24	-0.57π	3.16	3.68	0	3.12	3.76	π
Pedestrian crossing the LoS signal path	L	4.44	8.29	-0.497π	20	0.87	π	20	0.87	$-\pi$
	Q	8.99	7.46	0.5π	2.14	6.64	-0.236π	2.79	3.73	$-\pi$
	N	3.92	0.14	-0.013π	20	1.07	π	20	1.07	$-\pi$

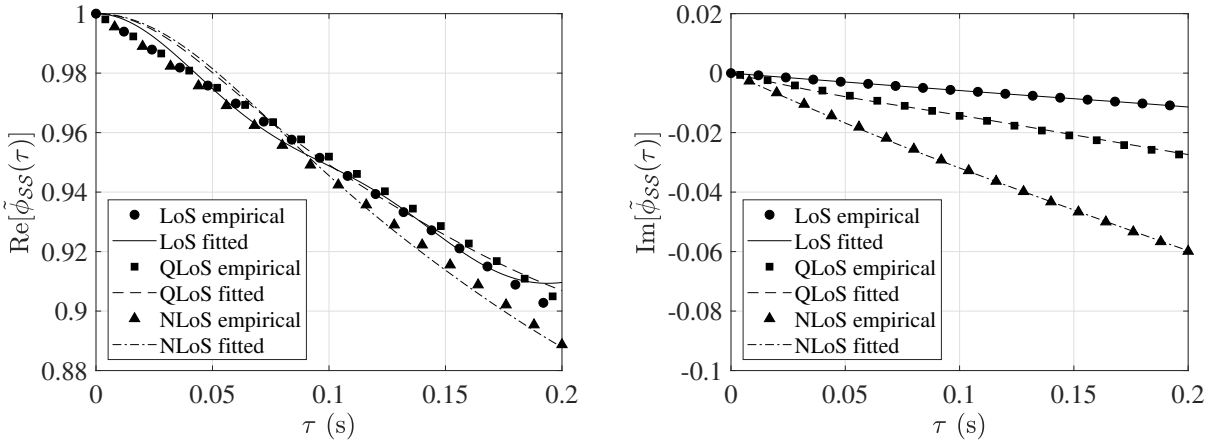

(a) Real part.

(b) Imaginary part.

Fig. 9: Empirical (shapes) and theoretical (lines) normalized complex ACFs for the rotating user experiment.

pedestrian moved far enough from the off-body link such that their movement no longer impacted the received signal. This progression can be seen from the normalized received signal time series in Fig. 10. For the first two seconds, the channel was in the LoS state with relatively small fluctuations in the received signal observed. From 2 s onwards, the variations in the received signal can be seen to increase as the pedestrian approached the optical LoS signal path between the TX and RX antennas, indicating that the channel had entered the QLoS state. At approximately 5.4 s a deep fade begins to occur corresponding to the NLoS state which was caused by the pedestrian's body blocking the direct signal path.

Similar to the rotating user example above, a dominant component was observed to be present in all three states. Also similar to the previous example, a reduction in the power contributed by the dominant component was observed to occur when transitioning from LoS through QLoS to NLoS channel conditions. One striking difference in the two scenarios considered was that the dominant component appeared to be less impacted by shadowing as shown by the estimates of k_{S_ι} (see Table II). Another interesting observation is that the power contributed by the scattered multipath was much lower in this experiment compared to when the user was rotating. A possible reason for this could be that the user (i.e., the human body phantom) significantly attenuated any scattered signal contribution arriving from behind the RX antenna whereas the rotational movement of the user in the previous example moved the RX antenna through the multipath field set up around the user. Contrasting with the previous example the LoS state occurred most often here. This was expected since the pedestrian blocked the direct signal path for a relatively short period within the experiment. A more striking observation here was that the PDF of the received signal envelope was unimodal. However unlike the Rayleigh and Rician fading models which are also unimodal, the underlying in-phase and quadrature components as well as the phase depart significantly from the unimodal case.

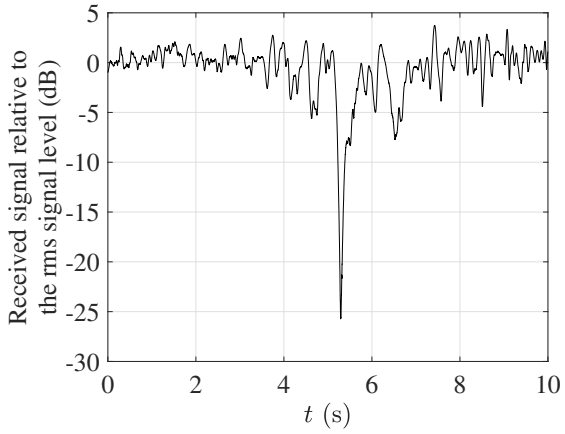

Fig. 10: Normalized received signal time series obtained during the pedestrian crossing the LoS signal path experiment.

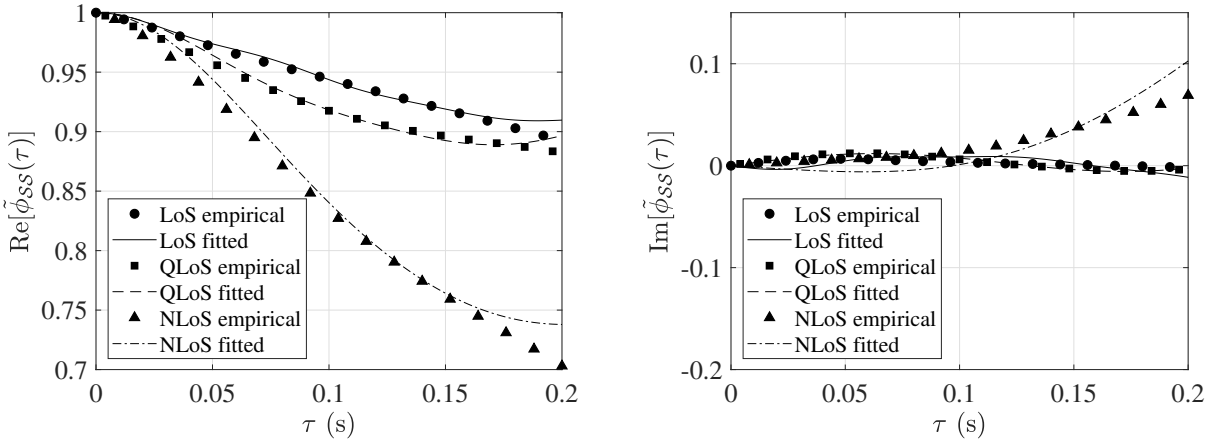

(a) Real part.

(b) Imaginary part.

Fig. 11: Empirical (shapes) and theoretical (lines) normalized complex ACFs for the pedestrian crossing the LoS signal path experiment.

The point is made that if this fading channel had been measured and characterized using only the received signal envelope, this important behavior may have been missed and subsequent inferences made about the in-phase, quadrature and phase components based upon Rayleigh or Rician fading (i.e., unimodal i.i.d. Gaussian quadrature components and uniform phase), could lead to the wrong conclusions and ultimately suboptimal wireless systems design. This can be seen from Fig. 8(c) where the best fit Rician PDF is also included for comparison. Visually, this also provides a satisfactory fit to the received signal envelope, however it reinforces the point that where possible, physical channel studies should include characterizations of the received signal in-phase and quadrature components as well as the received signal phase.

To fit the normalized state ACFs the first 2 s were used for the LoS state, the time series between 2 and 4 s for the QLoS state, whereas between 5.4 and 6.4 s were used for the NLoS state based on inspection of Fig. 10. All parameter estimates for each state are given in Table V. Fig. 11 shows the TSM received signal empirical normalized complex autocorrelation along with the fitted normalized ACFs (i.e., $\bar{r}_\iota = 1$) for the three states. It can be observed the TSM again provides a good fit across all three states for both the real and imaginary parts of the complex ACF. Strong correlation was observed to persist in the real part of the complex ACF over the considered time window for both the LoS and QLoS states. The real part of the complex ACF for the NLoS state showed moderate decay. However, the imaginary part of the complex ACF, was close to zero for the LoS and QLoS states, suggesting that the two quadrature components are largely uncorrelated when considered over this duration. The imaginary part of the complex ACF for the NLoS state showed increasing correlation near the end of the considered time window, indicating slightly increasing correlation between the in-phase and quadrature components. Finally, Fig. 11(a) shows that the real part of the complex ACF for the NLoS state decorrelates at a faster rate compared to the QLoS and LoS states. The NLoS state approaches a value of 0.7, whilst the QLoS and LoS states remain very strongly time correlated, reaching a value of approximately 0.9 by the end of the observation window.

V. Conclusion

In this paper, for the first time, we have unified LoS, QLoS and NLoS signal propagation under the umbrella of the proposed Three State Model. To this end, the TSM has been shown to have a strong physical motivation in relation to realistic scenarios encountered in practical communication scenarios. More precisely, within each of its constituent states, fading is assumed to follow that described by the Rician fading model, with one significant departure. That is the optional presence of a dominant component, which may or may not be shadowed. The shadowing in this case is assumed to follow a separate Rician distribution, allowing the TSM to be fully defined in terms of underlying Gaussian random variables. This has the benefit, that simulation of the TSM is relatively straightforward, further advocating its adoption as a comprehensive fading model. We have also derived many of the important first- and second-order statistics necessary for a complete characterization of the complex received signal envelope. This includes the PDFs of the in-phase and quadrature components, the joint envelope-phase, phase and received signal envelope as well as the complex ACF. A number of examples have been provided for these statistics alongside respective simulated results to demonstrate their validity.

Furthermore, two example applications have been provided for channels which are known to encounter the propagation phenomena encapsulated by the TSM. Using experimental data obtained for off-body communications channels which considered a rotating user and also the case where a pedestrian intersected the direct LoS signal path between the TX and RX, we have been able to show the excellent fit that that the TSM provides across all of the aforementioned statistics. Lastly it is shown that if only the received signal envelope is considered in channel measurements, departures from common assumptions such as unimodal in-phase and quadrature components and

uniform phase may be missed. This reinforces the use of the TSM for a richer characterization of fading, especially in scenarios where channels can be expected to alternate between LoS, QLoS and NLoS.

APPENDIX A
PROOF AND CLOSED-FORM SOLUTION FOR (19)

The model presented in (9) implies that when Z_ι is conditioned on ζ_ι, it follows a Gaussian distribution [37, eq. (2.3-8)]. To find the PDF of the in-phase or quadrature components for each of the individual states, ζ_ι is averaged over in the conditioned Z_ι, similar to [38, Appendix A], such that

$$f_{Z_\iota}(z_\iota) = \sqrt{\frac{1+k_\iota}{\pi\ \bar{r}_\iota^2}} \int_0^\infty \frac{f_{\zeta_\iota}(\zeta_\iota)}{\exp\left(\frac{(z_\iota-\zeta_\iota\lambda_\iota)^2(1+k_\iota)}{\bar{r}_\iota^2}\right)}\ d\zeta_\iota. \quad (37)$$

The integral in (37) can be solved by substituting (15) into (37), along with [46, eq. (8.447.1)], and applying the identities [46, eq. (3.462.1)] and [46, eq. (9.240)] sequentially to give (19).

A closed-form solution to (19) is found by taking (19), then using the primary definition of the confluent hypergeometric function [48, eq. (07.20.02.0001.01)], and [48, eq. (06.10.27.0001.01)], along with the definitions [58, eq. (1.3.22)], and [58, eq. (1.3.28)] provides

$$\begin{aligned} f_{Z_\iota}(z_\iota) = {} & \frac{\sqrt{1+k_\iota}\,(1+k_{S_\iota})}{\sqrt{\pi}\eta_\iota} \exp\left(-k_{S_\iota} - \frac{z_\iota^2(1+k_\iota)}{\bar{r}_\iota^2}\right) \\ & \times \left[\frac{2z_\iota\lambda_\iota\,(1+k_\iota)}{\sqrt{\eta_\iota}}\right. \\ & \times \Psi_2\left(\frac{3}{2};\frac{3}{2},1;\frac{(z_\iota\lambda_\iota(1+k_\iota))^2}{\bar{r}_\iota^2\eta_\iota},\epsilon\right) \\ & \left. + \bar{r}_\iota F^{1:0;0}_{0:1;0}\left(\begin{matrix}1:-;-;\\ -:\frac{1}{2};-;\end{matrix}\frac{(z_\iota\lambda_\iota(1+k_\iota))^2}{\bar{r}_\iota^2\eta_\iota},\epsilon\right)\right], \end{aligned} \quad (38)$$

where $F^{:::}_{:::}\left(\begin{smallmatrix}\cdot&\cdot&\cdot;&\cdot&\cdot&\cdot;\\ \cdot&\cdot&\cdot;&\cdot&\cdot&\cdot;\end{smallmatrix}\cdot,\cdot\right)$ denotes the generalized Kampé de Fériet function [58, eq. (1.3.28)], $\Psi_2(\cdot;\cdot,\cdot;\cdot,\cdot)$ is the confluent Appell function [58, eq. (1.3.22)] and $\epsilon = \frac{\bar{r}_\iota^2 k_{S_\iota}(1+k_{S_\iota})}{\eta_\iota}$.

APPENDIX B
PROOF AND CLOSED-FORM SOLUTION FOR (22)

Following the mathematical model for the individual states of the TSM given in (9), the PDF of the received signal envelope, R_ι, can be expressed as [59, Appendix A]

$$f_{R_\iota}(r_\iota) = \frac{r_\iota}{\sigma_\iota^2 \exp\left(\frac{r_\iota^2}{2\sigma_\iota^2}\right)} \int_0^\infty \frac{I_0\left(\frac{\zeta_\iota\delta_\iota r_\iota}{\sigma_\iota^2}\right)}{\exp\left(\frac{\zeta_\iota^2\delta_\iota^2}{2\sigma_\iota^2}\right)} f_{\zeta_\iota}(\zeta_\iota)\ d\zeta_\iota. \quad (39)$$

The integral in (39) can be solved by substituting (15), and using [46, eq. (8.447.1)], along with the necessary transformation of variables, and the identities [46, eq. (6.643.2)] and [46, eq. (9.220.2)]. Based on this and knowing (10) and $\delta_\iota^2 = 2\sigma_\iota^2 k_\iota$, (22) is obtained.

By using [48, eq. (07.20.02.0001.01)] and the identities [48, eq. (06.10.27.0001.01)] and [58, eq. (1.3.22)] in (22), a closed-form solution for the PDF of the received signal envelope in each state is found to be

$$\begin{aligned} f_{R_\iota}(r_\iota) = {} & \frac{2r_\iota(1+k_\iota)\mu_\iota}{\bar{r}_\iota^2} \exp\left(-k_{S_\iota} - \frac{r_\iota^2(1+k_\iota)}{\bar{r}_\iota^2}\right) \\ & \times \Psi_2\left(1;1,1;\frac{r_\iota^2 k_\iota(1+k_\iota)}{\bar{r}_\iota^2(1+k_\iota+k_{S_\iota})},k_{S_\iota}\mu_\iota\right). \end{aligned} \quad (40)$$

APPENDIX C
PROOF AND CLOSED-FORM SOLUTION FOR (25)

From the model definition in (9), it can be seen that, when conditioned on ζ_ι, X_ι and Y_ι are independent Gaussian RVs. Following from this, the joint conditional PDF can be written as,

$$f_{X_\iota,Y_\iota|\zeta_\iota}(x_\iota,y_\iota;\zeta_\iota) = f_{X_\iota|\zeta_\iota}(x_\iota;\zeta_\iota) \times f_{Y_\iota|\zeta_\iota}(y_\iota;\zeta_\iota). \quad (41)$$

Now using a Jacobian transformation, $|J_\iota| = r_\iota$, the conditional joint envelope-phase distribution is found as,

$$f_{R_\iota,\Theta_\iota|\zeta_\iota}(r_\iota,\theta_\iota;\zeta_\iota) = |J_\iota| f_{X_\iota,Y_\iota|\zeta_\iota}(x_\iota,y_\iota;\zeta_\iota). \quad (42)$$

Then, expressing x_ι and y_ι in terms of r_ι and θ_ι, using [46, eq. (8.447.1)], averaging over ζ_ι, using (15), and sequentially applying the identities [46, eq. (3.462.1)] and [46, eq. (9.240)], we obtain (25).

Taking the PDF of the joint envelope-phase given in (25) and applying the definitions [48, eq. (06.10.27.0001.01)] and [58, eq. (1.3.22)] results in

$$\begin{aligned} f_{R_\iota,\Theta_\iota}(r_\iota,\theta_\iota) = {} & \frac{r_\iota(1+k_\iota)\mu_\iota}{\pi\bar{r}_\iota^2} \exp\left(-k_{S_\iota} - \frac{r_\iota^2(1+k_\iota)}{\bar{r}_\iota^2}\right) \\ & \times \left[\Psi_2\left(1;\frac{1}{2},1;\frac{r_\iota^2(1+k_\iota)\Delta_\iota(\theta_\iota,\varpi_\iota)}{\bar{r}_\iota^2},k_{S_\iota}\mu_\iota\right)\right. \\ & + \frac{2r_\iota\sqrt{1+k_\iota}\sqrt{\Delta_\iota(\theta_\iota,\varpi_\iota)}}{\bar{r}_\iota} \\ & \left. \times \Psi_2\left(\frac{3}{2};\frac{3}{2},1;\frac{(1+k_\iota)\Delta_\iota(\theta_\iota,\varpi_\iota)}{r_\iota^{-2}\bar{r}_\iota^2},k_{S_\iota}\mu_\iota\right)\right]. \end{aligned} \quad (43)$$

APPENDIX D
PROOF AND CLOSED-FORM SOLUTION FOR (26)

Integrating the PDF of the joint envelope-phase in (25) with respect to the received signal envelope, R_ι, by first applying a quadratic transformation and using the identity [46, eq. (7.621.4)], which results in (26).

By using the PDF of the signal phase given in (26), the primary definition of the Gauss hypergeometric function [48, eq. (07.23.02.0001.01)], [48, eq. (06.10.27.0001.01)], [48, eq. (07.20.02.0001.01)], and [58, eq. (1.3.21)], the PDF of the signal phase is found to be

$$\begin{aligned} f_{\Theta_\iota}(\theta_\iota) = {} & \frac{\mu_\iota \exp(-k_{S_\iota})}{2\pi}\left[\Psi_1\left(1,1;\frac{1}{2},1;\Delta_\iota(\theta_\iota,\varpi_\iota),k_{S_\iota}\mu_\iota\right)\right. \\ & \left. + \frac{\pi\sqrt{\Delta_\iota(\theta_\iota,\varpi_\iota)}}{2(1-\Delta_\iota(\theta_\iota,\varpi_\iota))^{\frac{3}{2}}}\,{}_1F_1\left(\frac{3}{2};1;\frac{k_{S_\iota}\mu_\iota}{1-\Delta_\iota(\theta_\iota,\varpi_\iota)}\right)\right], \end{aligned} \quad (44)$$

with $\Psi_1(\cdot,\cdot;\cdot,\cdot;\cdot,\cdot)$ denoting the confluent Appell function [58, eq. (1.3.21)].

ACKNOWLEDGMENT

The work of D. Morales-Jimenez is supported in part by the State Research Agency (AEI) of Spain and the European Social Fund under grant RYC2020-030536-I and by AEI under grant PID2020-118139RB-I00.

REFERENCES

[1] A. F. Molisch, *Wireless Communications*, 2nd ed. Hoboken, NJ, USA: Wiley, 2011.

[2] T. S. Rappaport, *Wireless Communications: Principles and Practice*, 2nd ed. Upper Saddle River, NJ, USA: Prentice Hall, 2002.

[3] S. J. Ambroziak, L. M. Correia, R. J. Katulski, M. Mackowiak, C. Oliveira, J. Sadowski, and K. Turbic, "An off-body channel model for body area networks in indoor environments," *IEEE Trans. Antennas Propag.*, vol. 64, no. 9, pp. 4022–4035, Sep. 2016.

[4] M. Boban, T. Vinhoza, M. Ferreira, J. Barros, and O. K. Tonguz, "Impact of vehicles as obstacles in vehicular ad hoc networks," *IEEE J. Sel. Area Comm.*, vol. 29, no. 1, pp. 15–28, Jan. 2011.

[5] K. Guan, D. He, B. Ai, D. W. Matolak, Q. Wang, Z. Zhong, and T. Kürner, "5-GHz obstructed vehicle-to-vehicle channel characterization for internet of intelligent vehicles," *IEEE Internet Things J.*, vol. 6, no. 1, pp. 100–110, Feb. 2019.

[6] C.-L. Cheng and A. Zajić, "Characterization of propagation phenomena relevant for 300 GHz wireless data center links," *IEEE Trans. Antennas Propag.*, vol. 68, no. 2, pp. 1074–1087, Feb. 2020.

[7] E. R. Pelet, J. E. Salt, and G. Wells, "Effect of wind on foliage obstructed line-of-sight channel at 2.5 GHz," *IEEE Trans. Broadcast.*, vol. 50, no. 3, pp. 224–232, Sep. 2004.

[8] E. P. Moraes, J. Covolan, M. Buffalo, and L. R. Maciel, "WiMAX near LOS measurements and comparison with propagation models," in *Proc. 3rd Eur. Conf. Antennas Propag. (EuCAP)*, Mar. 2009, pp. 1–4.

[9] S. O. Rice, "Statistical properties of a sine wave plus random noise," *Bell Sys. Tech.*, vol. 27, no. 1, pp. 109–157, Jan. 1948.

[10] A. Abdi, W. C. Lau, M. S. Alouini, and M. Kaveh, "A new simple model for land mobile satellite channels: first- and second-order statistics," *IEEE Trans. Wireless Commun.*, vol. 2, no. 3, pp. 519–528, May 2003.

[11] R. F. Harrington, *Field Computation by Moment Methods*. New York, NY, USA: Wiley, 1993.

[12] J. M. Jin, *The Finite Element Method in Electromagnetics*, 2nd ed. New York, NY, USA: Wiley, 2002.

[13] A. Taflove and S. C. Hagness, *Computational Electrodynamics: The Finite-Difference Time-Domain Method*, 3rd ed. Norwood, MA, USA: Artech House, 2005.

[14] S. Halpern, "A study of environmental constraints in the coastal harbor radiotelephone system," *IEEE J. Ocean. Eng.*, vol. 2, no. 3, pp. 242–254, Jul. 1977.

[15] R. Bultitude, "Measurement, characterization and modeling of indoor 800/900 MHz radio channels for digital communications," *IEEE Commun. Mag.*, vol. 25, no. 6, pp. 5–12, Jun. 1987.

[16] A. R. Tharek and J. P. McGeehan, "Indoor propagation and bit error rate measurements at 60 GHz using phase-locked oscillators," in *Proc. 38th IEEE Veh. Technol. Conf. (VTC Spring)*, Jun. 1988, pp. 127–133.

[17] H. Xu, T. Rappaport, R. Boyle, and J. Schaffner, "Measurements and models for 38-GHz point-to-multipoint radiowave propagation," *IEEE J. Sel. Areas Commun.*, vol. 18, no. 3, pp. 310–321, Mar. 2000.

[18] J. Kivinen, X. Zhao, and P. Vainikainen, "Empirical characterization of wideband indoor radio channel at 5.3 GHz," *IEEE Trans. Antennas Propag.*, vol. 49, no. 8, pp. 1192–1203, Aug. 2001.

[19] J. Maurer, T. Fugen, and W. Wiesbeck, "Narrow-band measurement and analysis of the inter-vehicle transmission channel at 5.2 GHz," in *Proc. IEEE 55th Veh. Technol. Conf. (VTC Spring)*, vol. 3, May 2002, pp. 1274–1278.

[20] M. H. Hashim and S. Stavrou, "Measurements and modelling of wind influence on radiowave propagation through vegetation," *IEEE Trans. Wirel. Commun.*, vol. 5, no. 5, pp. 1055–1064, May 2006.

[21] S. L. Cotton and W. G. Scanlon, "Characterization and Modeling of the Indoor Radio Channel at 868 MHz for a Mobile Bodyworn Wireless Personal Area Network," *IEEE Antennas Wireless Propag. Lett.*, vol. 6, pp. 51–55, 2007.

[22] S. L. Cotton, G. A. Conway, and W. G. Scanlon, "A time-domain approach to the analysis and modeling of on-body propagation characteristics using synchronized measurements at 2.45 GHz," *IEEE Trans. Antennas Propag.*, vol. 57, no. 4, pp. 943–955, Apr. 2009.

[23] S. L. Cotton, "A statistical model for shadowed body-centric communications channels: Theory and validation," *IEEE Trans. Antennas Propag.*, vol. 62, no. 3, pp. 1416–1424, Mar. 2014.

[24] N. Bhargav, S. L. Cotton, and D. E. Simmons, "Secrecy capacity analysis over κ–μ fading channels: Theory and applications," *IEEE Trans. Commun.*, vol. 64, no. 7, pp. 3011–3024, Jul. 2016.

[25] S. L. Cotton, "Human body shadowing in cellular device-to-device communications: channel modeling using the shadowed κ-μ fading model," *IEEE J. Sel. Areas Commun.*, vol. 33, no. 1, pp. 111–119, Jan. 2015.

[26] I. Sen and D. W. Matolak, "Vehicle–vehicle channel models for the 5-GHz band," *IEEE Trans. Intell. Transp. Syst.*, vol. 9, no. 2, pp. 235–245, Jun. 2008.

[27] D. W. Matolak and J. Frolik, "Worse-than-Rayleigh fading: Experimental results and theoretical models," *IEEE Commun. Mag.*, vol. 49, no. 4, pp. 140–146, Apr. 2011.

[28] W. Khawaja, I. Guvenc, and D. Matolak, "UWB channel sounding and modeling for UAV air-to-ground propagation channels," in *Proc. IEEE Global Commun. Conf. (GLOBECOM)*, Dec. 2016, pp. 1–7.

[29] Z. Qiu, X. Chu, C. Calvo-Ramirez, C. Briso, and X. Yin, "Low altitude UAV air-to-ground channel measurement and modeling in semiurban environments," *Wireless Commun. and Mobile Computing*, vol. 2017, Nov. 2017.

[30] J. M. Romero-Jerez, F. J. Lopez-Martinez, J. F. Paris, and A. J. Goldsmith, "The fluctuating two-ray fading model: Statistical characterization and performance analysis," *IEEE Trans. Wireless Commun.*, vol. 16, no. 7, pp. 4420–4432, Jul. 2017.

[31] U. Fernandez-Plazaola, J. Lopez-Fernandez, J. F. Paris, and E. Martos-Naya, "A tractable fading channel model with two-sided bimodality," *IEEE Access*, vol. 7, pp. 99 928–99 936, 2019.

[32] E. N. Gilbert, "Capacity of a burst-noise channel," *Bell Syst. Tech. J.*, vol. 39, no. 5, pp. 1253–1265, Sep. 1960.

[33] E. O. Elliott, "Estimates of error rates for codes on burst-noise channels," *Bell Syst. Tech. J.*, vol. 42, no. 5, pp. 1977–1997, Sep. 1963.

[34] H. S. Wang and N. Moayeri, "Finite-state Markov channel-a useful model for radio communication channels," *IEEE Trans. Veh. Technol.*, vol. 44, no. 1, pp. 163–171, Feb. 1995.

[35] Q. Zhang and S. Kassam, "Finite-state Markov model for Rayleigh fading channels," *IEEE Trans. Commun.*, vol. 47, no. 11, pp. 1688–1692, Nov. 1999.

[36] D. Hess, "Cycle slipping in a first-order phase-locked loop," *IEEE Trans. Commun. Technol.*, vol. 16, no. 2, pp. 255–260, Apr. 1968.

[37] J. G. Proakis, *Digital Communications*, 4th ed. New York: McGraw-Hill, 2001.

[38] J. W. Browning, S. L. Cotton, D. Morales-Jimenez, and F. J. Lopez-Martinez, "The Rician complex envelope under line of sight shadowing," *IEEE Commun. Lett.*, vol. 23, no. 12, pp. 2182–2186, Dec. 2019.

[39] K. E. Baddour and N. C. Beaulieu, "Autoregressive modeling for fading channel simulation," *IEEE Trans. Wireless Commun.*, vol. 4, no. 4, pp. 1650–1662, Jul. 2005.

[40] A. G. Zajic and G. L. Stüber, "Space-time correlated mobile-to-mobile channels: Modelling and simulation," *IEEE Trans. Veh. Technol.*, vol. 57, no. 2, pp. 715–726, Mar. 2008.

[41] A. Abdi, J. A. Barger, and M. Kaveh, "A parametric model for the distribution of the angle of arrival and the associated correlation function and power spectrum at the mobile station," *IEEE Trans. Veh. Technol.*, vol. 51, no. 3, pp. 425–434, May 2002.

[42] J. W. Browning, S. L. Cotton, P. C. Sofotasios, D. Morales-Jimenez, and M. D. Yacoub, "LoS, Non-LoS and Quasi-LoS signal propagation: A three state channel model," in *Proc. IEEE 95th Veh. Technol. Conf. (VTC Spring)*, Jun. 2022, pp. 1–5.

[43] M. D. Yacoub, *Foundations of Mobile Radio Engineering*, 1st ed. Boca Raton, USA: CRC Press, 1993.

[44] T. Aulin, "A modified model for the fading signal at a mobile radio channel," *IEEE Trans. Veh. Technol.*, vol. 28, no. 3, pp. 182–203, Aug. 1979.

[45] G. L. Stüber, *Principles of Mobile Communication*, 3rd ed. Springer, 2011.

[46] I. S. Gradshteyn and I. M. Ryzhik, *Table of Integrals, Series, and Products*, 7th ed. San Diego, CA, USA: Academic Press, 2007.

[47] I. Dey, G. G. Messier, and S. Magierowski, "Joint fading and shadowing model for large office indoor WLAN environments," *IEEE Trans. Antennas Propag.*, vol. 62, no. 4, pp. 2209–2222, Apr. 2014.

[48] "Wolfram Research, Inc." accessed on 03/25/2019. [Online]. Available: http://functions.wolfram.com/

[49] G. Fraidenraich, J. C. S. S. Filho, and M. D. Yacoub, "Second-order statistics of maximal-ratio and equal-gain combining in Hoyt fading," *IEEE Commun. Lett.*, vol. 9, no. 1, pp. 19–21, Jan. 2005.

[50] L. Wang, W. Liu, and Y. Cheng, "Statistical analysis of a mobile-to-mobile Rician fading channel model," *IEEE Trans. Veh. Technol.*, vol. 58, no. 1, pp. 32–38, Jan. 2009.

[51] K. Baddour and N. Beaulieu, "Accurate simulation of multiple cross-correlated Rician fading channels," *IEEE Trans. Commun.*, vol. 52, no. 11, pp. 1980–1987, Nov. 2004.

[52] A. Trivedi and R. Gupta, "On the analysis of envelope correlation and spectra for Rician fading channel," *Wireless Pers. Commun.*, vol. 47, no. 2, pp. 281–292, Oct. 2008.

[53] R. H. Clarke, "A statistical theory of mobile-radio reception," *Bell Syst. Tech. J.*, vol. 47, no. 6, pp. 957–1000, Jul. 1968.

[54] A. S. Akki and F. Haber, "A statistical model of mobile-to-mobile land communication channel," *IEEE Trans. Veh. Technol.*, vol. 35, no. 1, pp. 2–7, Feb. 1986.

[55] S. K. Yoo, S. L. Cotton, P. C. Sofotasios, and S. Freear, "Shadowed fading in indoor off-body communication channels: A statistical characterization using the κ-μ/gamma composite fading model," *IEEE Trans. Wireless Commun.*, vol. 15, no. 8, pp. 5231–5244, Aug. 2016.

[56] S. L. Cotton, A. McKernan, A. J. Ali, and W. G. Scanlon, "An experimental study on the impact of human body shadowing in off-body communications channels at 2.45 GHz," in *Proc. 5th Eur. Conf. Antennas Propag. (EuCAP)*, Apr. 2011, pp. 3133–3137.

[57] G. A. Conway and W. G. Scanlon, "Antennas for over-body-surface communication at 2.45 GHz," *IEEE Trans. Antennas Propag.*, vol. 57, no. 4, pp. 844–855, Apr. 2009.

[58] H. M. Srivastava and P. W. Karlsson, *Multiple Gaussian Hypergeometric Series*. John Wiley & Sons, 1985.

[59] N. Simmons, C. R. N. D. Silva, S. L. Cotton, P. C. Sofotasios, S. K. Yoo, and M. D. Yacoub, "On shadowing the κ-μ fading model," *IEEE Access*, vol. 8, pp. 120 513–120 536, 2020.

Jonathan W. Browning (Member, IEEE) received the M.Eng. degree in electrical and electronic engineering and the Ph.D. degree in electrical engineering from the Queen's University of Belfast, U.K., in 2017 and 2022, respectively. Since 2021 he is a Connected Learning Tutor with the school of electronics, electrical engineering and computer science within the Queen's University of Belfast. His research interests include channel characterization and modeling, and wireless communications in general.

Simon L. Cotton (Senior Member, IEEE) received the B.Eng. degree in electronics and software from Ulster University, Ulster, U.K., in 2004, and the Ph.D. degree in electrical and electronic engineering from the Queen's University of Belfast, Belfast, U.K., in 2007. From 2007 to 2011 he was a Research Fellow, then Senior Research Fellow, 2011 to 2012, Lecturer (Assistant Professor), 2012 to 2015, and Reader (Associate Professor), 2015 to 2019 at the Queen's University of Belfast. He is currently a Full Professor and the Director of the Centre for Wireless Innovation (CWI), Queen's University Belfast. Professor Cotton has authored and co-authored over 150 publications in major IEEE/IET journals and refereed international conferences, three book chapters, and two patents. Among his research interests are propagation measurements and statistical channel characterization. His other research interests include cellular device-to-device, vehicular, and body-centric communications. Professor Cotton was awarded the H. A. Wheeler Prize, in July 2010, by the IEEE Antennas and Propagation Society for the best applications journal paper in the IEEE TRANSACTIONS ON ANTENNAS AND PROPAGATION during 2009. In July 2011, he was awarded the Sir George Macfarlane Award from the U.K. Royal Academy of Engineering in recognition of his technical and scientific attainment since graduating from his first degree in engineering.

Paschalis C. Sofotasios (Senior Member, IEEE) was born in Volos, Greece, in 1978. He received the M.Eng. degree from Newcastle University, U.K., in 2004, the M.Sc. degree from the University of Surrey, U.K., in 2006, and the Ph.D. degree from the University of Leeds, U.K., in 2011. He has held positions at the University of Leeds, University of California at Los Angeles, USA, Tampere University of Technology, Finland, Aristotle University of Thessaloniki, Greece and Khalifa University, UAE, where he is currently an Associate Professor with the Department of Electrical Engineering and Computer Science. He has received the scholarship from UK-EPSRC for his M.Sc. studies and from UK-EPSRC and Pace plc for his Ph.D. studies. His research interests are concerned with topics relating to physical layer digital and optical communications, in which he has published extensively in IEEE journals and conferences. He is a regular reviewer of several international journals and a member of the technical program committee of numerous IEEE conferences. He received the Exemplary Reviewer Award from the IEEE COMMUNICATIONS LETTERS in 2012 and from IEEE TRANSACTIONS ON COMMUNICATIONS in 2015 and 2016. He was an Editor of IEEE COMMUNICATIONS LETTERS from 2016 until 2021 and a TPC Co-Chair of the Communication Theory Symposium of IEEE Globecom 2020. He is a Senior Member IEEE and he received the Best Paper Award in IEEE ICUFN 2013.

David Morales-Jimenez (Senior Member, IEEE) is an RyC Research Professor with the Department of Signal Theory, Networking and Communications at University of Granada (Spain). He received the M.Sc. and Ph.D. degrees in Telecommunication Technologies from University of Malaga (Spain) in 2008 and 2011, respectively. Between 2011 and 2013 he was a Postdoctoral Fellow at Universitat Pompeu Fabra (Barcelona, Spain). He then joined the Hong Kong University of Science and Technology (HKUST), first as Visiting Scholar (2014-2016) and then as Research Assistant Professor (2016–2018) with the Department of Electronic and Computer Engineering. He was a Lecturer (Assistant Professor) at Queen's University Belfast (2018–2021) and an Associate Professor at University of Malaga (2021–2022). He also held visiting appointments at University College London (Electronic and Electrical Engineering, 2010) and at Stanford University (Statistics Department, 2015). His research interests include statistical signal processing, random matrix theory, and high-dimensional statistics, with multidisciplinary applications to wireless communications and computational biology.

Prof. Morales is an Associate Editor of the IEEE TRANSACTIONS ON SIGNAL PROCESSING and an Elected Member of the IEEE Technical Committee on Signal Processing for Communications and Networking (SPCOM). He received the Best Ph.D. Thesis Award in Electrical and Computer Engineering by the University of Malaga. He and his coauthors received the Best 'Statistica Sinica' paper award at Joint Statistical Meetings 2020. He was a Poster Co-Chair of the IEEE Communication Theory Workshop 2022 and a General Co-Chair of the IEEE Spanish Workshop on Signal Processing, Information Theory and Communications 2022.

Michael Daoud Yacoub (Member, IEEE) was born in Brazil, in 1955. He received the B.S.E.E. and M.Sc. degrees from the School of Electrical and Computer Engineering, State University of Campinas (UNICAMP), Campinas, São Paulo, Brazil, in 1978 and 1983, respectively, and the Ph.D. degree from the University of Essex, U.K., in 1988. From 1978 to 1985, he was a Research Specialist in the development of the Tropico digital exchange family with the Research and Development Center of Telebras, Brazil. In 1989, he joined the School of Electrical and Computer Engineering, UNICAMP, where he is currently a Full Professor. He consults for several operating companies and industries in the wireless communications area. He is the author of *Foundations of Mobile Radio Engineering* (Boca Raton, FL: CRC, 1993), *Wireless Technology: Protocols, Standards, and Techniques* (Boca Raton, FL: CRC, 2001), and the coauthor of the *Telecommunications: Principles and Trends* (São Paulo, Brazil: Erica, 1997, in Portuguese). He holds two patents. His general research interest includes wireless communications.